COMMUNICATIONS PHYSICS

ARTICLE

https://doi.org/10.1038/s42005-020-0394-3 OPEN

Interferometric and fluorescence analysis of shock wave effects on cell membrane

Yusuke Ito [1], David Veysset [2,3], Steven E. Kooi[3], Dmitro Martynowych[2,3], Keiichi Nakagawa [4,5]✉ & Keith A. Nelson[2,3]✉

Shock waves generated by laser pulses have been gaining attention for biological and medical applications in which shock-induced cell membrane deformation influences cell permeation. However, the mechanisms through which the deformation of cell membranes affects permeability remain mostly unknown because of the difficulty of observing in real time the transient and dynamic behaviors of the shock waves and the cells. Here we present an all-optical measurement method that can quantitatively capture the pressure distribution of the propagating shock wave and simultaneously monitor the dynamic behavior of cell membranes. Using this method, we find that the profile of the shock wave dictates the cell membrane permeation. The results suggest a possible mechanism of membrane permeation where sharp pressure gradients create pores on the membrane. Our measurement will foster further understanding of the interaction of shock waves with cells, while the proposed mechanism advances biological and medical applications of shock waves.

[1] Department of Mechanical Engineering, The University of Tokyo, Tokyo 113-8656, Japan. [2] Department of Chemistry, Massachusetts Institute of Technology, Cambridge, MA 02139, USA. [3] Institute for Soldier Nanotechnologies, Massachusetts Institute of Technology, Cambridge, MA 02139, USA. [4] Department of Bioengineering, The University of Tokyo, Tokyo 113-8656, Japan. [5] Department of Precision Engineering, The University of Tokyo, Tokyo 113-8656, Japan. ✉email: kei@bmpe.t.u-tokyo.ac.jp; kanelson@mit.edu

Biological and medical applications of shock waves have been attracting interest in both clinical and scientific studies[1–3]. The applications involve a broad range of techniques, such as damage induction on cancer cells[4,5], delivery of DNA vaccines or anticancer chemotherapeutics into diseased cells[6,7], treatment of tissues[3,8], and transformation of filamentous fungi[9–11] and bacteria[12–15]. The cell membrane, which works as a barrier and also as a gate between the interior of a cell and outside environment, plays an important role in mediating such physiological effects. Membranes are sensitive to mechanical force and expected to deform under the mechanical constraints resulting from the interaction with a shock[16,17]. However, because the direct observation of the interaction in real time has not been achieved, the determinative mechanisms causing the membrane permeation remain largely unclear.

Better understanding has been impeded by the incompatibility of conventional medical shock wave devices based on piezoelectric, electrohydraulic, or electromagnetic methods[8] or of hydrophone measurement of underwater shock profiles[18] with direct real-time observation of individual cells as they interact with and respond to shock. Additionally, in biological studies, shock waves are commonly generated in petri dishes or vials containing a number of cells in a culture solution, and the effects of shock waves are investigated after removing the culture solution[19], preventing monitoring of the dynamic behavior of individual cells. In contrast, shock waves generated by focused ultrashort laser pulses can be microscopically targeted[4,6,19,20] and synchronized with real-time optical probes.

Here we present an optically-based system that can produce controlled shock waves on a microscopic scale, acquire the shock pressure distribution quantitatively, and monitor the dynamic behavior of cell membranes in response to shock. Our measurements allow changes of cell membranes to be associated with quantitative characteristics of shock waves.

Results

Experimental method. Figure 1 shows the experimental setup. We generated planar shock waves by cylindrically focusing the pump laser beam into a line, as illustrated in Fig. 1a. A picosecond laser pump pulse (amplified Ti:sapphire system, 300-ps duration, 800-nm wavelength) was focused into a thin phosphate-buffered saline (PBS) liquid layer that included carbon nanoparticles, fluorescent dyes, and HeLa cells. Using a cylindrical lens with a 200-mm focal length and an achromatic doublet with a 30-mm focal length, as shown in Fig. 1b, the focused laser line had a length of 750 μm and a width of 6 μm. The liquid was confined between 100-μm-thick and 200-μm-thick glass windows separated by a 10-μm polymer spacer, yielding a 10–20-μm thick liquid layer. Upon laser absorption by the carbon nanoparticles, two counter-propagating planar shock waves were generated in the liquid layer and remained mostly confined in the plane due to the impedance mismatch between the liquid and the glass substrates[21].

To perform quantitative measurement of the shock pressure distribution with both high spatial and temporal resolution, interferometric images were acquired with a Mach-Zehnder interferometer and a variably-delayed probe laser pulse. The probe pulse, generated by another amplified Ti:sapphire system (150-fs pulse duration, 400-nm wavelength), was synchronized with the pump pulse and delivered to the liquid layer colinearly with the pump pulse, as shown in Fig. 1b. The time delay between the pump and the probe pulses was adjusted using a delay generator controlling the timing of the two laser systems. Because the jitter of the synchronization was 20 ns, the time difference between the pump and probe pulses was measured by photodetectors in every experiment. By comparing the interferograms obtained before and after the generation of shock waves, the change in refractive index induced by the density change in the liquid following the shock front was directly extracted. Note that a short probe pulse duration was necessary to avoid blurring of the shock image, but precise timing between the pump and probe pulses was not needed.

To visualize the dynamic behavior of the cell membrane, we distributed outside the cells fluorescent dyes having no cell membrane permeability under normal conditions. The membrane was observed as the interface between fluorescent and dark regions. Transport of dye molecules from outside to inside the cells resulting from shock-induced membrane permeability was observed as the appearance and increase of fluorescence inside the cell. In this study, fluorescein isothiocyanate (FITC) dextran of average molecular weight 3000–5000 Da was used; the molecules can permeate into cells when the size of the pores on

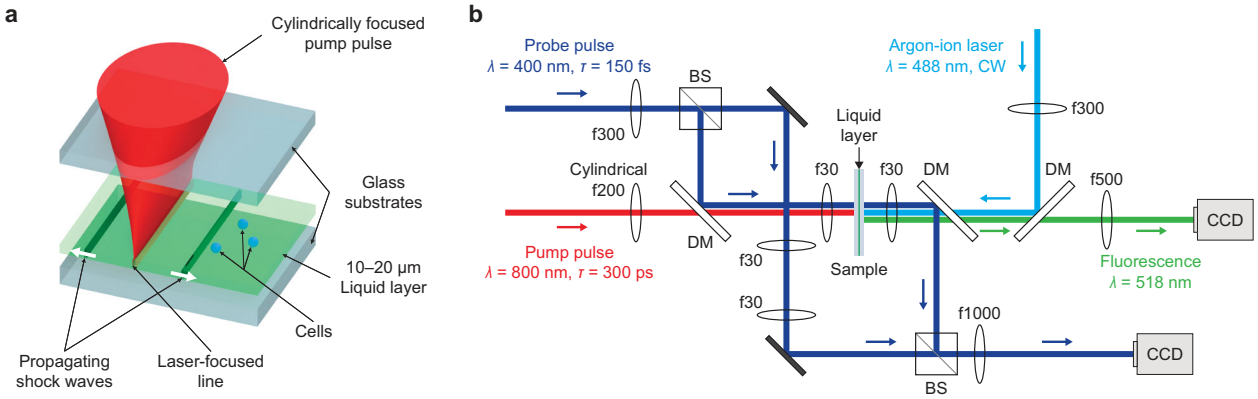

Fig. 1 Optical apparatus for analyzing cell membrane interactions with and responses to shock. a Sample assembly. Cells are placed in a thin liquid layer that contains fluorescent dyes. A cylindrically focused pump pulse (red beam) irradiates a line in the plane of the liquid layer. Two counter-propagating shock waves are launched and remain confined in the plane. **b** Optical setup. A cylindrical-lens configuration shapes the pump pulse into a line focus. Interferometric imaging is performed using a Mach-Zehnder configuration and a variably-delayed probe pulse (blue beams). The probe beam is split into two arms and recombined using two beam splitters (BS). The sample plane is imaged onto a charge-coupled device (CCD) using a two-lens telescope. A continuous-wave (CW) argon-ion-laser beam (azure) is delivered to the sample plane through a dichroic mirror (DM) to induce dye fluorescence (green) which is imaged onto another CCD. For each laser and fluorescence, λ is the wavelength. τ is the pulse duration of each laser. The focal length of lens is indicated such as f300 where 300 is measured in millimeters.

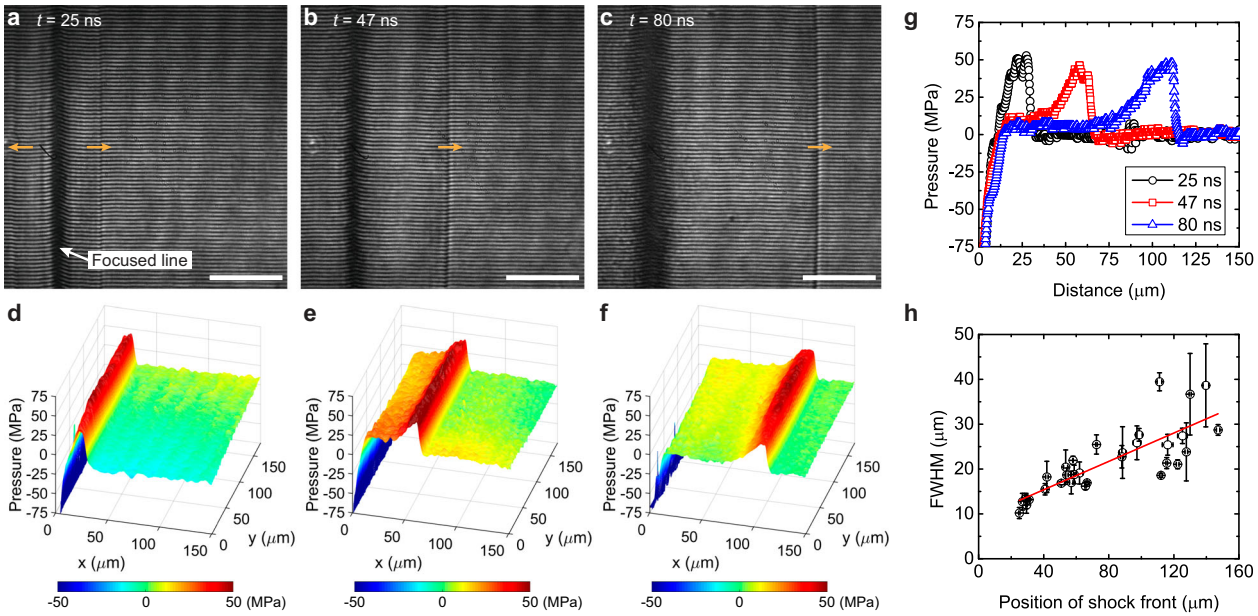

Fig. 2 Interferograms and analyzed shock waveforms. a–c Interferometric images showing shock wave propagation at three different time delays *t*. Arrows indicate the propagation direction of the shock fronts. Bubbles are formed at the laser focused area and appear as a black line on the images. Each image was recorded from a different sample region. Scale bars, 50 μm. **d–f** Spatial distributions of pressure extracted from **a–c**, respectively. **g** Comparison of shock waveforms at different time delays as a function of the distance from the laser-focused line. **h** Full width at half maximum (FWHM) of each shock waveform as a function of the position of shock front with respect to the laser-focused line. The error bars indicate the standard deviation.

cells becomes larger than that of FITC dextran. The fluorescent molecules were excited by a continuous-wave argon-ion-laser beam with a wavelength of 488 nm. Light was emitted with a wavelength of 518 nm and separated from the excitation light using a dichroic mirror. This in situ monitoring was conducted in real time with a high-sensitivity charge-coupled device (CCD) camera.

Interferometric analysis. Interferograms of shock waves propagating in the liquid (in the absence of cells) were recorded to characterize the shock waves generated in our setup. Figure 2a–c shows images recorded with increasing probe pulse delays at a pump pulse energy of 200 ± 50 μJ. The shock fronts are observable as distortions in the interferogram fringes. To quantitatively analyze the pressure profile of the shock, the interferometric images were converted to 2D phase images through a 2D Fourier transform method with a Hann function for spectrum apodization[22]. After phase unwrapping, 2D phase images were obtained before and after laser excitation and subtracted to obtain the optical phase change profile (see Supplementary Fig. 1 and Supplementary Note 1). The extracted phase change $\Delta\varphi$ was converted to the change in refractive index Δn based on the relation

$$\Delta n = \frac{\Delta\varphi}{2\pi}\frac{\lambda}{l}, \quad (1)$$

where λ is the wavelength of the probe pulse and l is the thickness of the liquid layer. The thickness of the liquid layer ranged from 10 to 20 μm. Although the polymer spacer between the glass substrates was 10-μm thick, distortion of the substrates caused the variation of the liquid layer thickness. Therefore, the thickness within the imaging field of view was measured before each experiment with an uncertainty of 1.4 μm. The change in the refractive index Δn was then translated into density change $\Delta\rho$:

$$\Delta\rho = \frac{\Delta n}{0.322}[\mathrm{g\ cm^{-3}}] \quad (2)$$

using an empirically determined formula for water[23], valid under shock conditions for densities ranging from 1.00 to 1.21 g cm^{-3}. Shock pressures associated with the measured density changes were calculated using the Tait equation of state of water[24]. The uncertainty of the pressures is related to the uncertainty of the density changes, which mainly originated from the uncertainty of the liquid thickness l.

The calculated pressure distributions with various time delays corresponding to the three images in Fig. 2a–c are shown respectively in Fig. 2d–f. $x = 0$ μm corresponds to the position at the laser-focused line. The pressure drop near $x = 0$ μm was caused by temperature increase (see Supplementary Fig. 2 and Supplementary Note 2 for details). The shock waveforms along the horizontal line defined by the multiple arrows in Fig. 2a–c are plotted in Fig. 2g. The peak pressures at 25, 47, and 80 ns were 52.8 ± 8.2, 46.3 ± 4.8, and 47.7 ± 3.5 MPa, corresponding to density changes of 23.3 ± 3.3 mg cm^{-3}, 20.6 ± 2.0 mg cm^{-3}, and 21.1 ± 1.5 mg cm^{-3}, respectively. The full widths at half maximum (FWHM) of the shock waveforms were 13.2 ± 0.2 μm, 16.2 ± 0.8 μm, and 21.3 ± 1.2 μm, respectively. The shock wave propagated with a speed of 1458 ± 15 m s^{-1}, which corresponded to the acoustic speed in water (≈1450 m s^{-1}) (see Supplementary Fig. 3a and Supplementary Note 3 for details).

The FWHM of each shock waveform at different propagation distance is plotted in Fig. 2h. It expanded as the shock wave propagated. According to the linear fitting shown as the red line, the initial FWHM at the laser-focused line was estimated to be 9.1 μm, and it expanded with the slope of 0.16. The peak pressures of shock waves at different propagation distances had large variations (see Supplementary Fig. 3b and Supplementary Note 3 for details) because of the fluctuations of the thickness of the liquid layer and the pump pulse energy. Despite the large variations in the peak pressures, the FWHM consistently indicated the clear (and well-known[25]) lengthening of the tail of the shock wave with propagation.

Fluorescence analysis. To monitor the dynamic behavior of cell membrane simultaneously with interferometric imaging of the

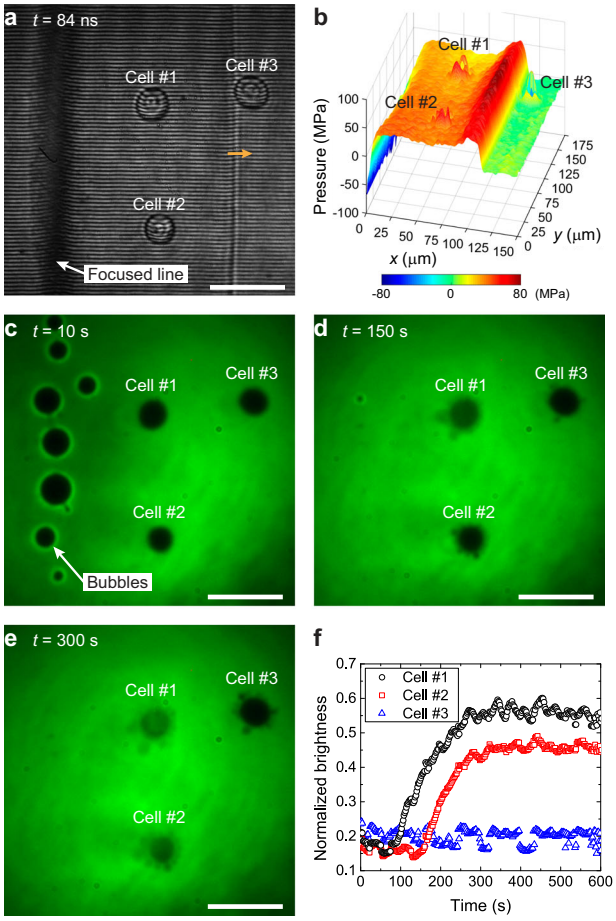

Fig. 3 Interferometric and fluorescence analysis. a Interferometric image showing a propagating shock wave and three cells with a time delay of 84 ns. An arrow indicates the propagation direction of the shock front. Scale bar, 50 μm. **b** Extracted spatial distribution of pressure. **c**–**e** Fluorescence images showing the permeation behavior of the fluorescent molecules into the cells. Images were recorded **c** 10 s, **d** 150 s, and **e** 300 s after the pump pulse was delivered (time indicated by *t*). Scale bars, 50 μm. **f** Normalized brightness inside the cells with increasing time after delivering the pump pulse obtained by fluorescence imaging.

shock, fluorescence imaging was used. Images were recorded for 300 s or longer with a frame rate of 0.5 Hz in a single experiment. An interferogram recorded 84 ns after the pump pulse irradiated the liquid layer, where cells are present, is shown in Fig. 3a. The pressure distribution extracted from the interferogram is shown in Fig. 3b. The pressure distribution indicates that the shock wave propagated with no visible disturbance after encountering the cell; the impedance mismatch between the water and the cell being small, the shock was not reflected or attenuated significantly by the cell[26]. The difference between the pressure distributions (peak pressure and pressure at the tail) shown in Figs. 2d–f and 3b arises from the fluctuations of the thickness of the liquid layer and the pump pulse energy independent from the presence of the cells. As shown in Fig. 3c–e, we captured the permeation behavior of the fluorescent molecules into the cells after cell-shock interaction, from which membrane disruption can be inferred arguably at scales below the optical resolution. The laser-focused line observed in Fig. 3a evolved after 10 s into large bubbles (Fig. 3c and Supplementary Fig. 4) that collapsed prior to 150 s (Fig. 3d). Bubbles normally collapse much faster in conventional experiments when they are not constrained[27]; however, because the bubbles were sandwiched between glass walls in our setup, the capillary forces prevented them from collapsing on a much shorter time scale. As time increased, the brightness inside cells #1 and #2, labeled in Fig. 3, increased. The increase in the brightness indicates that pores were generated in the cell membranes, and that fluorescent molecules permeated the cell membranes when the pore size increased sufficiently. Pores can be generated due to a non-uniform pressure distribution on the membrane[28]. Blebs, the cellular protrusions, were observed around all three cells after the shock wave passed as shown in Fig. 3d, e. Blebbing occurs due to local rupture of membrane–cytoskeleton attachments in regions of high pressure in cells[29]. Therefore, the results may indicate that the pressure is unequally distributed and locally increased on the membrane during the passage of the shock wave. The brightness changes inside the cells were plotted in Fig. 3f by averaging the brightness inside each cell and normalizing it by comparing the brightness inside and outside the cell. In cells #1 and #2, the brightness started to increase 94 s and 158 s after the shock, respectively, and saturated at ~300 s. Permeation was not observed in cell #3 throughout the observation.

Discussion

Despite the slight difference between the locations of cells #1 and #2, the time-dependences of their brightness changes differed substantially. The difference may stem from either variability between the cells or in the shock properties. To identify the origin, we measured the brightness changes of 53 cells located at different distances away from laser-focused lines in order to investigate the time dependence of permeation behavior at different distances from the shock excitation region.

The results shown in Fig. 4a clearly indicate that the closer the cells were located to the laser-focused line, the faster the brightness of the cells increased. Because Fig. 2h showed that FWHM of the shock waveform increased with the propagation of the shock wave, the FWHM may affect the brightness change. To verify this hypothesis, the cells were divided into two groups; one with permeation of the fluorescent molecules at 300 s after the shock delivery and the other without permeation. As shown in Fig. 4b, the two groups were compared after calculating the FWHM at the position of each cell (see Supplementary Fig. 5 and

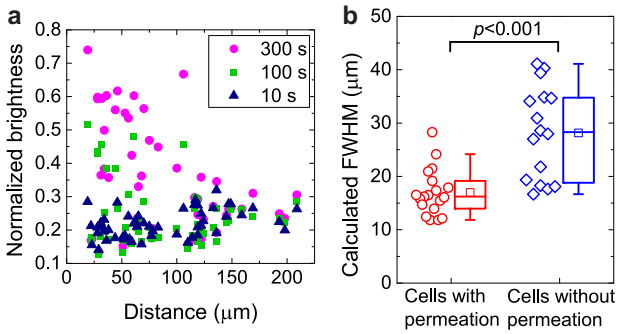

Fig. 4 Effect of a shock wave on cell permeation. a Normalized brightness inside each cell located at different distance away from the laser-focused line and at increasing time after the pump pulse was delivered. **b** Comparison of full width at half maximum (FWHM) of shock waveform at the position of each cell belonging to one of two groups: with permeation ($n = 19$ cells, red circles) and without permeation ($n = 16$ cells, blue diamonds) of fluorescent molecules at 300 s after the pump pulse was delivered. The box plot shows the middle value of the data set (central line), the 25th percentile (bottom of the box), and the 75th percentile (top of the box) with a set of whiskers determined by the 1.5 interquartile ranges. Data were compared by conducting a two-tailed *t*-test using all data points and by calculating the probability value (*p* value).

Supplementary Note 4 for details). The results of a *t*-test demonstrated that there was a significant difference between the two groups regarding the FWHM. When the propagation distance is under 70 μm, the FWHM is typically smaller than the diameter of the cells (~20 μm). Therefore, this suggests that at short distance the shock wave is narrow enough to create both low- and high-pressure regions within a cell during the passage of the wave. This non-uniform pressure distribution creates pores on the membrane, resulting in fluorescent molecule penetration into the cell through the pores. On the other hand, when the propagation distance of the shock wave becomes larger, the FWHM typically exceeds the diameter of the cells. In this situation, the cell cytoplasm is more homogeneously compressed and released rather than being affected by the gradient of the pressure field in the cell during the passage of the shock wave, therefore limiting pore formation in the cell membrane and preserving the membrane impermeability to the fluorescent molecules. This explains why permeation was not observed in cell #3 in Fig. 3f. Although microjets and secondary shock waves can be generated when the bubbles collapse[30,31], the cells were located away from the laser-focused line, and therefore, the bubble collapse is expected to little effect on the cells. In addition, we anticipate capillary effects to slow down bubble collapse (or prevent it entirely), consequently reducing the emission of secondary shock wave.

Because most conventional methods could not analyze the influence of shock pressure distribution on individual cells, the key parameter causing membrane permeation has not been clarified. Although previous studies[32–34] suggested the contribution of peak pressure, rise time or impulse, direct evaluation through quantitative analysis of the shock profile has not been achieved. Conversely, our method allows such analyses which demonstrate the crucial effect of FWHM. We anticipate that future studies considering different shock parameters, as well as cell conditions, will advance the understanding of the mechanisms leading to membrane permeation. Regarding shock parameters, modulating the spatial and temporal profiles of the laser pulse will permit control of not only the FWHM but also the peak pressure, rise time, fall time, impulse and number of shocks. Because our system allows the generation of shock waves and quantitative analyses of shock parameters and cell permeability at the same time, the shock parameters can be further optimized through direct observations. The optimization will contribute to the more effective use of shock waves in the biotechnological and clinical applications.

In summary, we have presented an all-optical measurement system that can produce a planer shock wave whose spatial profile, propagation through cells, and effects on cell membrane behavior can be monitored. Our results demonstrate the influence of the profile of the shock wave on membrane permeation, where shocks that are shorter temporally and spatially are more likely to make cells permeable to fluorescent dye. The results suggest a possible mechanism of membrane permeation due to sharp pressure gradients, i.e. non-uniform pressure distribution in the cell that deforms cell membranes and causes pore formation. Our all-optical measurement will foster further understanding of the interaction of shock waves with cells, while the proposed mechanism may guide the formulation of optimal conditions for biological and medical applications of shock waves.

Methods

Sample preparation. The liquid sample was made by mixing a 0.4 wt% carbon nanoparticles, a 2 wt% of FITC dextran of average molecular weight 3000–5000 Da (FD4, Sigma-Aldrich®), and cells in PBS (Sigma-Aldrich®). The carbon concentration was yielded by diluting black ink (Winsor & Newton Ink®) 50x in PBS. The liquid was enclosed between a 100 μm-thick and a 200 μm-thick, 1 inch-diameter, glass substrates (Schott D263®). A photoresist (SU-8 2015, MicroChem®) was coated and developed on the 200-μm-thick substrate to form a ring-patterned spacer. The spacer had an outer diameter of 22 mm, an inner diameter of 19 mm, and a thickness of 10 μm to ensure separation between the substrates.

Cell preparation. HeLa cells were maintained in DMEM supplemented with 10% (v/v) fetal bovine serum and 1% (v/v) Pen Strep at 37 °C and 5% CO_2 in a T-75 flask. When the cells reached ~80% confluence, the growth media was aspirated. Trypsin-EDTA 0.25% (2 mL) was added to the cells and incubated for 15 min at 37 °C and 5% CO_2. To quench the trypsin, DMEM supplemented with 10% (v/v) fetal bovine serum and 1% (v/v) Pen Strep (8 mL) was added to the flask. In all, 7.5 mL of the dissociated cells in media were transferred to a 15 mL falcon tube and spun at 500 rcf for 3 min. The supernatant was removed and the pellet was resuspended in 250 μL of PBS.

Sample characterization. The thickness of the liquid layer was calculated according to the Beer-Lambert law. The thickness l can be expressed as

$$l = -\frac{1}{\alpha_1}\log_{10}\left(\frac{I - I_B}{I_0 - I_B}\right), \quad (3)$$

where α_1 is the absorption coefficient of the liquid, I and I_0 are the brightness detected by a CCD after the probe pulses transmitted through the liquid sample and a pure water in the glass substrates, respectively, and I_B is the brightness of the background without the probe pulses. $\alpha_1 = 93\ \mathrm{cm}^{-1}$ was measured for the wavelength of 400 nm using a UV-VIS spectrometer. The effect of the reflection by the glass surfaces on the accuracy of the thickness measurement was canceled by using the same glass substrates for the brightness measurements of the liquid sample and the pure water. For canceling the variation of the probe pulse energies and the noise from the CCD, the exposure time of the CCD was set to 20 ms, so that the variation and the noise were averaged by the 20 probe pulses with a repetition rate of 1 kHz. The thickness was calculated by the brightness of each pixel on the CCD and averaged. A standard deviation of the thickness was measured to be 1.4 μm. It was calculated by comparing the 20 different images taken by moving the sample a few micrometers in a plane before the experiments.

Normalization of brightness. For the normalization, the average of the brightness of 100 pixels inside each cell was divided by a reference brightness, which was the average of the brightness of 100 pixels outside the cell. The reference area was 10 μm away from each cell. The brightness inside the cells was above zero before the generation of the shock, because the fluorescence from the fluorescent molecules existing between the cells and the glass substrate was detected.

Reporting summary. Further information on research design is available in the Nature Research Reporting Summary linked to this article.

Data availability

The data that support the findings of this work are available from the corresponding author upon reasonable request.

Code availability

The codes used for the data collection and analysis are available from the corresponding author upon reasonable request.

Received: 10 March 2020; Accepted: 17 June 2020;
Published online: 08 July 2020

References

1. Seah, B. C.-Q. & Teo, B. M. Recent advances in ultrasound-based transdermal drug delivery. *Int. J. Nanomed.* **13**, 7749–7763 (2018).
2. Battula, N., Menezes, V. & Hosseini, H. A miniature shock wave driven microjet injector for needle-free vaccine/drug delivery. *Biotechnol. Bioeng.* **113**, 2507–2512 (2016).
3. Mani-Babu, S., Morrissey, D., Waugh, C., Screen, H. & Barton, C. The effectiveness of extracorporeal shock wave therapy in lower limb tendinopathy. *Am. J. Sports Med.* **43**, 752–761 (2015).
4. Steinhauser, M. O. & Schmidt, M. Destruction of cancer cells by laser-induced shock waves: recent developments in experimental treatments and multiscale computer simulations. *Soft Matter* **10**, 4778–4788 (2014).
5. Moosavi-Nejad, S. F., Hosseini, S. H. R., Satoh, M. & Takayama, K. Shock wave induced cytoskeletal and morphological deformations in a human renal carcinoma cell line. *Cancer Sci.* **97**, 296–304 (2006).
6. Tirlapur, U. K. & König, K. Cell biology: targeted transfection by femtosecond laser. *Nature* **418**, 290–291 (2002).

7. Azagury, A., Khoury, L., Enden, G. & Kost, J. Ultrasound mediated transdermal drug delivery. *Adv. Drug Deliv. Rev.* **72**, 127–143 (2014).
8. Zelle, B. A., Gollwitzer, H., Zlowodzki, M. & Bühren, V. Extracorporeal shock wave therapy: current evidence. *J. Orthop. Trauma* **24**, S66–S70 (2010).
9. Magaña-Ortíz, D. et al. A novel and highly efficient method for genetic transformation of fungi employing shock waves. *Fungal Genet. Biol.* **56**, 9–16 (2013).
10. Gómez-Lim, M. A., Ortíz, D. M., Fernández, F. & Loske, A. M. *Transformation of Fungi Using Shock Waves*, 209–219 (Springer, Cham, 2015). https://doi.org/10.1007/978-3-319-10142-2_21
11. Loske, A. M. *Medical and Biomedical Applications of Shock Waves*. (Springer, Cham, 2017). https://doi.org/10.1007/978-3-319-47570-7
12. Jagadeesh, G., Nataraja, K. & Udayakumar, M. Shock waves can enhance bacterial transformation with plasmid DNA. *Curr. Sci.* **87**, 734–735 (2004).
13. Divya Prakash, G., Anish, R. V., Jagadeesh, G. & Chakravortty, D. Bacterial transformation using micro-shock waves. *Anal. Biochem.* **419**, 292–301 (2011).
14. Loske, A. M., Campos-Guillen, J., Fernández, F. & Castaño-Tostado, E. Enhanced shock wave-assisted transformation of Escherichia coli. *Ultrasound Med. Biol.* **37**, 502–510 (2011).
15. Campos-Guillén, J., Fernández, F., Pastrana, X. & Loske, A. M. Relationship between plasmid size and shock wave-mediated bacterial transformation. *Ultrasound Med. Biol.* **38**, 1078–1084 (2012).
16. Steinbach, P., Hofstädter, F., Nicolai, H., Rössler, W. & Wieland, W. In vitro investigations on cellular damage induced by high energy shock waves. *Ultrasound Med. Biol.* **18**, 691–699 (1992).
17. Ohl, C.-D. & Wolfrum, B. Detachment and sonoporation of adherent HeLa-cells by shock wave-induced cavitation. *Biochim. Biophys. Acta Gen. Subj.* **1624**, 131–138 (2003).
18. Schoeffmann, H., Schmidt-Kloiber, H. & Reichel, E. Time-resolved investigations of laser-induced shock waves in water by use of polyvinylidenefluoride hydrophones. *J. Appl. Phys.* **63**, 46–51 (1988).
19. Chakravarty, P., Qian, W., El-Sayed, M. A. & Prausnitz, M. R. Delivery of molecules into cells using carbon nanoparticles activated by femtosecond laser pulses. *Nat. Nanotechnol.* **5**, 607–611 (2010).
20. Antkowiak, M., Torres-Mapa, M. L., Stevenson, D. J., Dholakia, K. & Gunn-Moore, F. J. Femtosecond optical transfection of individual mammalian cells. *Nat. Protoc.* **8**, 1216–1233 (2013).
21. Veysset, D., Maznev, A. A., Pezeril, T., Kooi, S. & Nelson, K. A. Interferometric analysis of laser-driven cylindrically focusing shock waves in a thin liquid layer. *Sci. Rep.* **6**, 24 (2016).
22. Takeda, M. & Mutoh, K. Fourier transform profilometry for the automatic measurement of 3-D object shapes. *Appl. Opt.* **22**, 3977 (1983).
23. Yadav, H. S. et al. Measurement of refractive index of water under high dynamic pressures. *J. Appl. Phys.* **44**, 2197–2200 (1973).
24. Gojani, A. B., Ohtani, K., Takayama, K. & Hosseini, S. H. R. Shock Hugoniot and equations of states of water, castor oil, and aqueous solutions of sodium chloride, sucrose and gelatin. *Shock Waves* **26**, 63–68 (2016).
25. Pezeril, T. et al. Direct visualization of laser-driven focusing shock waves. *Phys. Rev. Lett.* **106**, 214503 (2011).
26. Kobayashi, K., Yoshida, S., Saijo, Y. & Hozumi, N. Acoustic impedance microscopy for biological tissue characterization. *Ultrasonics* **54**, 1922–1928 (2014).
27. Akhatov, I. et al. Collapse and rebound of a laser-induced cavitation bubble. *Phys. Fluids* **13**, 2805–2819 (2001).
28. Adhikari, U., Goliaei, A. & Berkowitz, M. L. Mechanism of membrane poration by shock wave induced nanobubble collapse: a molecular dynamics study. *J. Phys. Chem. B* **119**, 6225–6234 (2015).
29. Charras, G. T., Yarrow, J. C., Horton, M. A., Mahadevan, L. & Mitchison, T. J. Non-equilibration of hydrostatic pressure in blebbing cells. *Nature* **435**, 365–369 (2005).
30. Lauterborn, W. & Vogel, A. Shock wave emission by laser generated bubbles. in *Bubble Dynamics and Shock Waves*, 67–103 (Springer, Berlin, 2013). https://doi.org/10.1007/978-3-642-34297-4_3
31. Li, Z. G., Liu, A. Q., Klaseboer, E., Zhang, J. B. & Ohl, C. D. Single cell membrane poration by bubble-induced microjets in a microfluidic chip. *Lab Chip* **13**, 1144–1150 (2013).
32. Doukas, A. G. & Flotte, T. J. Physical characteristics and biological effects of laser-induced stress waves. *Ultrasound Med. Biol.* **22**, 151–164 (1996).
33. Mulholland, S. E., Lee, S., McAuliffe, D. J. & Doukas, A. G. Cell loading with laser-generated stress waves: the role of the stress gradient. *Pharm. Res.* **16**, 514–518 (1999).
34. Kodama, T., Hamblin, M. R. & Doukas, A. G. Cytoplasmic molecular delivery with shock waves: importance of impulse. *Biophys. J.* **79**, 1821–1832 (2000).

Acknowledgements

We thank A. A. Maznev (MIT, USA) for discussion on the project, and C. Fadzen and B. Pentelute (MIT, USA) for sample preparation. This material is based upon work supported in part by the U. S. Army Research Office through the Institute for Soldier Nanotechnologies, under Cooperative Agreement Number W911NF-18-2-0048.

Author contributions

D.V., K.N., and K.A.N. designed the experiments. Y.I., D.V., S.E.K., and K.N. constructed the experimental setup. Y.I. and K.N. conducted the experiments. D.V. developed the code to extract the pressure distribution from the interferogram. Y.I. analyzed the data. D.M. aided in performing experiments and interpreting the results. D.V., K.N., and K.A.N. supervised the work. Y.I. wrote the paper and all authors contributed to improvement of the paper.

Competing interests

The authors declare no competing interests.

Additional information

Supplementary information is available for this paper at https://doi.org/10.1038/s42005-020-0394-3.

Correspondence and requests for materials should be addressed to K.N. or K.A.N.

Reprints and permission information is available at http://www.nature.com/reprints

Publisher's note Springer Nature remains neutral with regard to jurisdictional claims in published maps and institutional affiliations.